

Temperature-insensitive fiber-optic refractive index sensor based on cascaded in-line interferometer and microwave photonics interrogation system

Xun Cai,^{a,b} Yi Zhuang,^{a,b} Tongtong Xie,^{a,b} Shichen Zheng,^{a,b} and Hongyan Fu^{a,b,*}

^aXiamen University, Department of Electronic Engineering, Xiamen, China

^bXiamen University, Fujian Key Laboratory of Ultrafast Laser Technology and Applications, Xiamen, China

Abstract. A compact and high-resolution fiber-optic refractive index (RI) sensor based on a microwave photonic filter (MPF) is proposed and experimentally validated. The sensing head utilizes a cascaded in-line interferometer fabricated by an input single-mode fiber (SMF) tapered fusion with no-core fiber-thin-core fiber (TCF)-SMF. The surrounding RI (SRI) can be demodulated by tracing the passband's central frequency of the MPF, which is constructed by the cascaded in-line interferometer, electro-optic modulator, and a section of dispersion compensation fiber. The sensitivity of the sensor is tailorable through the use of different lengths of TCF. Experimental results reveal that with a 30 mm length of TCF, the sensor achieves a maximum theoretical sensitivity and resolution of -1.403 GHz/refractive index unit (RIU) and 1.425×10^{-7} RIU, respectively, which is at least 6.3 times higher than what has been reported previously. Furthermore, the sensor exhibits temperature-insensitive characteristics within the range of $25^\circ\text{C} - 75^\circ\text{C}$, with a temperature-induced frequency change of only ± 1.5 MHz. This value is significantly lower than the frequency change induced by changes in the SRI. The proposed MPF-based cascaded in-line interferometer RI sensor possesses benefits such as easy manufacture, low cost, high resolution, and temperature insensitivity.

Keywords: fiber-optic sensor; microwave photonics; frequency demodulation; Mach-Zehnder interferometer.

Received Dec. 19, 2023; revised manuscript received May 8, 2024; accepted for publication Jun. 12, 2024; published online Jul. 12, 2024.

© The Authors. Published by SPIE and CLP under a Creative Commons Attribution 4.0 International License. Distribution or reproduction of this work in whole or in part requires full attribution of the original publication, including its DOI.

[DOI: [10.1117/1.APN.3.4.046011](https://doi.org/10.1117/1.APN.3.4.046011)]

1 Introduction

Refractive index (RI) sensing holds significant promise in the fields of biomedicine, chemistry, and environmental protection.¹⁻³ Despite the high resolution offered by traditional instruments such as the Abbe refractometer, their large size and weight pose drawbacks. Consequently, there is a pressing need for a miniaturized, high-resolution alternative capable of real-time measurements. Over the past two decades, fiber-optic RI sensors have gained rapid traction due to their advantages, such as compactness, corrosion resistance, electromagnetic immunity, and light weight. To accurately measure the surrounding RI (SRI), various sensors have been successively proposed,

including fiber Bragg grating (FBG),⁴ tilted fiber Bragg grating (TFBG),^{5,6} long-period fiber grating (LPFG),⁷ surface plasmon resonance (SPR),⁸ lossy mode resonance^{9,10} and fiber interferometric sensing.^{11,12} Among these, the last type has gained significant attention for its merits of high sensitivity, low cost, and easy fabrication.

In addition, three primary demodulation methods for measuring SRI exist, i.e., wavelength demodulation, intensity demodulation, and frequency demodulation. The commonly used wavelength demodulation scheme involves combining an optical spectrum analyzer (OSA) and fiber-optic interferometers. Li et al.¹³ proposed a modal interferometer that utilizes thin-core fiber (TCF) and photonic crystal fiber (PCF), achieving a sensitivity of 48.9 nm/refractive index unit (RIU) within 1.34 – 1.4 RIU. Wang et al.¹⁴ demonstrated a miniature fiber-

*Address all correspondence to Hongyan Fu, fuhongyan@xmu.edu.cn

optics Mach–Zehnder interferometer (MZI) based on near-surface gap-coupled waveguide structure manufactured by a femtosecond laser. The achieved sensitivity is -59.90238 nm/RIU within $1.34 - 1.42$ RIU. Despite these advancements, the wavelength demodulation methods usually face challenges such as poor resolution (currently, the most advanced OSA resolution is 0.01 nm) and high system cost. Furthermore, intensity demodulation is widely used in RI sensing, with solutions such as the multicore fiber structure presented by Mumtaz et al.,¹⁵ offering a sensitivity of 178.2 dB/RIU from 1.334 to 1.37 RIU. However, due to issues such as light-source fluctuation and polarization fading effects in the system, the intensity demodulation-based solutions, while cost-effective, require further development before being produced. To address the challenges in the demodulation methods mentioned above, the scheme based on frequency demodulation emerges,^{16–19} such as microwave photonics (MWP) filter and optoelectronic oscillator. By leveraging the high-resolution measurement capabilities of digital signal processors for microwave signals, optic fiber sensors based on MWP techniques hold promise for enhancing sensing performance, including resolution and demodulation time. The fundamental idea of the MWP sensing system is the concept of converting minute changes in the wavelength domain into substantial frequency shifts in the microwave domain. Cao et al.²⁰ revealed a temperature-compensational human epidermal growth factor receptor 2 (HER2) antigen detection based on microwave photonic filter (MPF) with a resolution of 2.45×10^{-6} RIU. Shi et al.²¹ proposed an RI sensor based on an etched phase-shifted fiber Bragg grating and an optoelectronic oscillator. The obtained sensitivity is 530 MHz/RIU after data processing.

In this paper, we have demonstrated an RI sensor based on SMF (taper) no-core fiber (NCF)-TCF-SMF structure and MWP interrogation system. The frequency demodulation method addresses the problems of high system cost and limited resolution associated with traditional wavelength domain demodulation. The proposed approach stands out by combining a miniaturized

and compact in-line MZI with MPF. By introducing a Vernier-like effect through tapered splicing, we effectively address the challenge of achieving high sensitivity while extending the sensing range, which is a limitation in traditional Vernier-based schemes (wavelength demodulation scheme). Comprehensive studies have been conducted with three different lengths of TCF concerning SRI, temperature, and stability. With the lengths of NCF and TCF set at 1 and 30 mm, respectively, the sensor achieves a maximum sensitivity and resolution of -1.403 GHz/RIU and 1.425×10^{-7} RIU, respectively. Moreover, the temperature-induced frequency change is only ± 1.5 MHz, indicating that the cross-effect error caused by temperature change is only 1.069×10^{-3} RIU.

2 Experimental Setup and Theoretical Analysis

Figure 1 illustrates the experimental configuration of the proposed RI sensing system, implemented with SMF (taper) NCF-TCF-SMF (STNTS) structure and MPF. The system utilized a broadband optical source (BOS) emitting light within the wavelength range of $1450 - 1650$ nm. Then, the light is coupled into the sensor head following its passage through an isolator (ISO). An OSA (resolution: 0.08 nm) is used to record the interference pattern, which is then modulated by an electro-optic modulator (EOM). The radio-frequency port of EOM is connected with port 1 of a vector network analyzer (VNA), with its electrode biased by a voltage source. The modulated light undergoes delay and amplification through a dispersion compensation fiber (DCF) and erbium-doped fiber amplifier (EDFA), respectively. Finally, the frequency response of the system can be observed on the VNA after the light is detected by a photodiode (PD).

The schematic diagram of the proposed fiber-optic RI sensor is shown in the upper part of Fig. 1. The input SMF is fusion-spliced with a 1 mm length of NCF using the Manual Mode of

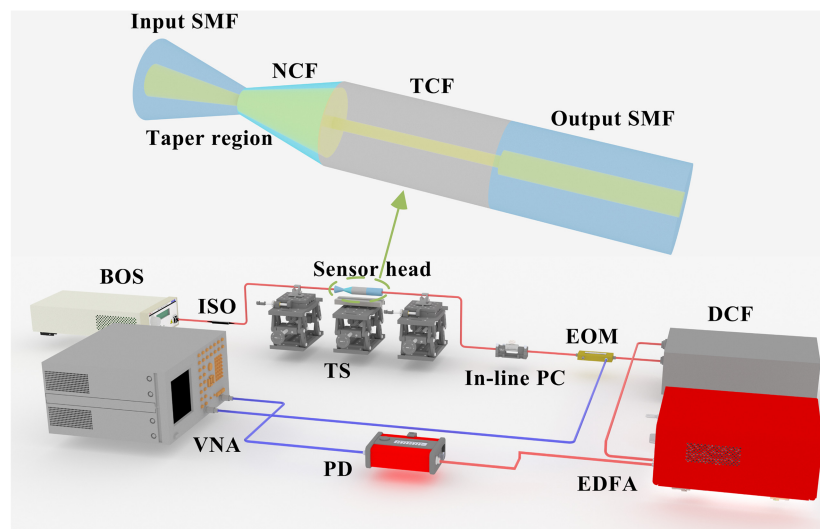


Fig. 1 Experimental configuration of the proposed RI sensor based on cascaded in-line interferometer and MWP interrogation system. SMF, single-mode fiber; NCF, no-core fiber; TCF, thin-core fiber; BOS, broadband optical source; ISO, isolator; TS, translation stage; PC, polarization controller; EDFA, Er-doped fiber amplifier; EOM, electro-optic modulator; DCF, dispersion compensation fiber; PD, photodiode; VNA, vector network analyzer.

the splicer (Fujikura, 66S, Tokyo, Japan). The parameters for this process are arc discharge intensity Standard-15 bit (1500 ms) and a tapered fusion splice speed of 30 bits. Subsequently, the AUTO Mode of the splicer is employed to fuse it with a section of TCF and the output SMF to form the STNTS structure. Introducing the taper region aims to enhance the sensitivity of the sensor to external physical parameters. However, considering factors such as mechanical strength, the length of the taper region should be a manageable length. In addition, to minimize the insertion loss of the sensing head and improve the visibility of the interference spectrum, each fiber section needs to be carefully cut with a fiber cleaver (Fujikura, CT-08) to obtain an optimal fiber end face with an angle of less than 2 deg.

When light enters the NCF from the input SMF, the fundamental mode in the SMF decomposes into numerous high-order modes in the NCF, forming a multimode interferometer (MMI). After passing through the tapered region, some light exists as leaky modes and disappears in the air, while the remainder enters the TCF. Due to the mode field mismatch effect, a small portion of modes are coupled into the excited cladding mode of the TCF, while the majority of light continues along the TCF's core, facilitated by the large numerical aperture (NA) value (0.42) of the TCF. A MZI is formed in the NCF-TCF-SMF section because of the existence of an optical path difference between the core and cladding of the TCF. Based on the above theoretical analysis, assuming there are no changes in mode polarization, the transmission function of the STNTS structure can be formulated as²²

$$\begin{aligned} T &= T_{\text{MMI}} \times T_{\text{MZI}} = \frac{1}{2}(1 + A_1 \cos \theta_1) \times \frac{1}{2}(1 + A_2 \cos \theta_2) \\ &= \frac{1}{4} \left[1 + A_1 \cos \theta_1 + A_2 \cos \theta_2 + \frac{1}{2} A_1 A_2 \cos(\theta_1 + \theta_2) \right. \\ &\quad \left. + \frac{1}{2} A_1 A_2 \cos(\theta_1 - \theta_2) \right], \end{aligned} \quad (1)$$

where $A_j (j = 1, 2)$ represent the visibilities of MMI and MZI, respectively. $\theta_i (i = 1, 2)$ denote the phase differences between the core mode and the dominant cladding mode that pass through the entire sensing head, which are given by

$$\theta_i = \frac{2\pi(n_{\text{core}}^{\text{eff}} - n_{\text{clad},i}^{\text{eff}})L_i}{\lambda}, \quad (2)$$

where $n_{\text{core}}^{\text{eff}}$ and $n_{\text{clad},i}^{\text{eff}}$ represent the effective RIs (ERIs) of the core mode and the dominant cladding mode of MMI and MZI, respectively. $L_i (i = 1, 2)$ are the lengths of the tapered region and TCF. λ represents the wavelength of input light. For $\theta_i = (2k + 1)\pi$, ($k = 1, 2, 3, \dots$), the dip wavelength could be shown as

$$\lambda_{\text{dip}} = \frac{2(n_{\text{core}}^{\text{eff}} - n_{\text{clad},i}^{\text{eff}})L_i}{2k + 1}. \quad (3)$$

When the SRI increases, the effective cladding RI $n_{\text{clad},i}^{\text{eff}}$ will increase correspondingly, and neither the taper region's nor the TCF's core are in contact with the outside, so it can be considered that the core's ERI $n_{\text{core}}^{\text{eff}}$ remains unchanged. Therefore, the ERI difference $\Delta n_i = n_{\text{core}}^{\text{eff}} - n_{\text{clad},i}^{\text{eff}}$ will decrease, and the wavelength of the transmission spectrum will be blueshifted. On the other hand, the expression for the free spectral range (FSR) is

$$\text{FSR} \approx \frac{\lambda^2}{\Delta n_i L_i} = \frac{\lambda^2}{(n_{\text{core}}^{\text{eff}} - n_{\text{clad},i}^{\text{eff}})L_i}. \quad (4)$$

It can be seen from Eq. (1) that the cascaded fiber interferometer has multiple frequency components, namely, θ_1 , θ_2 , $\theta_1 + \theta_2$, and $\theta_1 - \theta_2$. Traditional schemes based on optical domain demodulation usually use the inverse fast Fourier transform method or the envelope extraction method to filter out the envelope components representing the entire interference envelope, aiming to obtain sensitivities-enhanced sensors through the Vernier effect.^{23,24} However, this method usually has some problems, such as a large demodulated wavelength recognition error, an unclear envelope pattern, bad interference spectrum uniformity, and low signal-to-noise ratio. To solve these drawbacks, a microwave photonics interrogation system (MPIS) based on STNTS and a frequency demodulation scheme is introduced in this paper. The central frequency of the MWP filter passband can be shown as

$$f = \frac{1}{DL_{\text{DCF}} \times \text{FSR}} = \frac{(n_{\text{core}}^{\text{eff}} - n_{\text{clad},i}^{\text{eff}})L_i}{DL_{\text{DCF}}\lambda^2}, \quad (5)$$

where D and L_{DCF} represent the dispersion coefficient and length of DCF, respectively. Taking the derivative of Eq. (5), it is found that the SRI-induced frequency sensitivity is about

$$\frac{df}{d\text{SRI}} = -\frac{dn_{\text{clad},i}^{\text{eff}}}{d\text{SRI}} \times \frac{L_i}{DL_{\text{DCF}}\lambda^2}. \quad (6)$$

From Eqs. (4)–(6), it can be seen that when the ERI difference is small, it will lead to an increase in FSR, resulting in the blueshift of the passband frequency. In addition, the sensitivity of the sensor is not only proportional to the cladding mode sensitivity $\frac{dn_{\text{clad},i}^{\text{eff}}}{d\text{SRI}}$ and sensing fiber's length L_i but also inversely proportional to the dispersion value of the DCF. This means that sensing systems with tailorable sensitivity can be made according to the demands of the practical application. Moreover, it should be noted that higher-order cladding modes usually have higher sensitivity values because the higher the order, the larger the mode field area and, therefore, are more susceptible to changes in the SRI.²⁵

3 Results and Discussions

Before conducting the sensing experiment, we carried out a preliminary study on the influence of tapered fiber length on the interference spectrum. Figure 2(a) shows the transmission spectra when the length of NCF (1 mm) and TCF (10 mm) remains unchanged and the length of the taper region of the STNTS structure varies at 100, 200, and 300 μm . The FSRs in all cases are ~ 3.85 nm, but the visibilities differ, measuring 5.38, 2.34, and 15.91 dB. The discrepancy in visibility can be attributed to the fact that with a longer taper region, more high-order modes can be excited, leading to a higher mode power ratio. Therefore, to ensure the high visibility for the sensor, the taper region lengths of the proposed sensor were all set to 300 μm . Figures 2(b) and 2(c) are the microscope images of the taper-NCF and TCF-SMF parts, respectively. It is important to note that while the insertion loss range of the samples is between -18 and -15 dB, attributed to the additional taper region, this level of loss is typically acceptable in optical fiber sensing

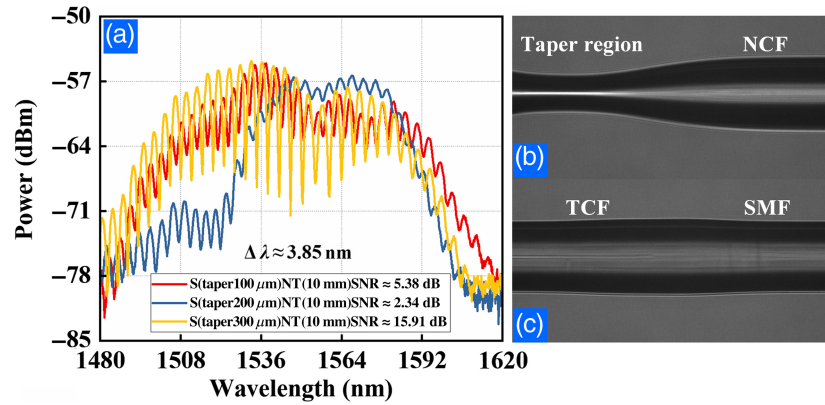


Fig. 2 (a) Interference spectra of the STNTS structure with different tapers' lengths and the same length of TCF. (b), (c) The microscope images of the fabricated MZI near two ends, respectively.

systems. In our experiment, as long as the insertion loss of the sensor remains within an acceptable range, typically less than -25 dB, the optical signal can be effectively amplified by an EDFA to ensure the performance of the entire sensing system. This ensures that the overall performance of the entire sensing system is maintained at a satisfactory level.

3.1 RI Sensing Experiment

In our experiment, three individual cascaded interferometers are constructed with TCFs of different lengths, i.e., 20, 25, and 30 mm. The selection of TCF length is crucial; if too short, the effective length of the optical wave is insufficient to induce a Vernier effect-like effect. The RI reagent employed in the

experiment was a glycerol solution of different concentrations (1.332 – 1.412 RIU), whose RI values were calibrated by a commercial refractometer with a resolution of 0.001 RIU. Two ends of the sensor were secured on two x -axis translation stages (TSS), which, in turn, were locked on two z -axis TSS, respectively. During the RI sensing process, the sensor head is fully immersed in a V-groove filled with glycerin solution. The surface underwent repeated rinsing with deionized water and alcohol until the response curves observed on the OSA and VNA aligned with those observed in the air.

Figure 3(a) shows that when the bias current of the BOS is 350 mA and the TCF is 20 mm, the visibility of the interference spectrum is greater than 15 dB within the range of 1.332 – 1.412 RIU. Figure 3(b) depicts the spectra obtained

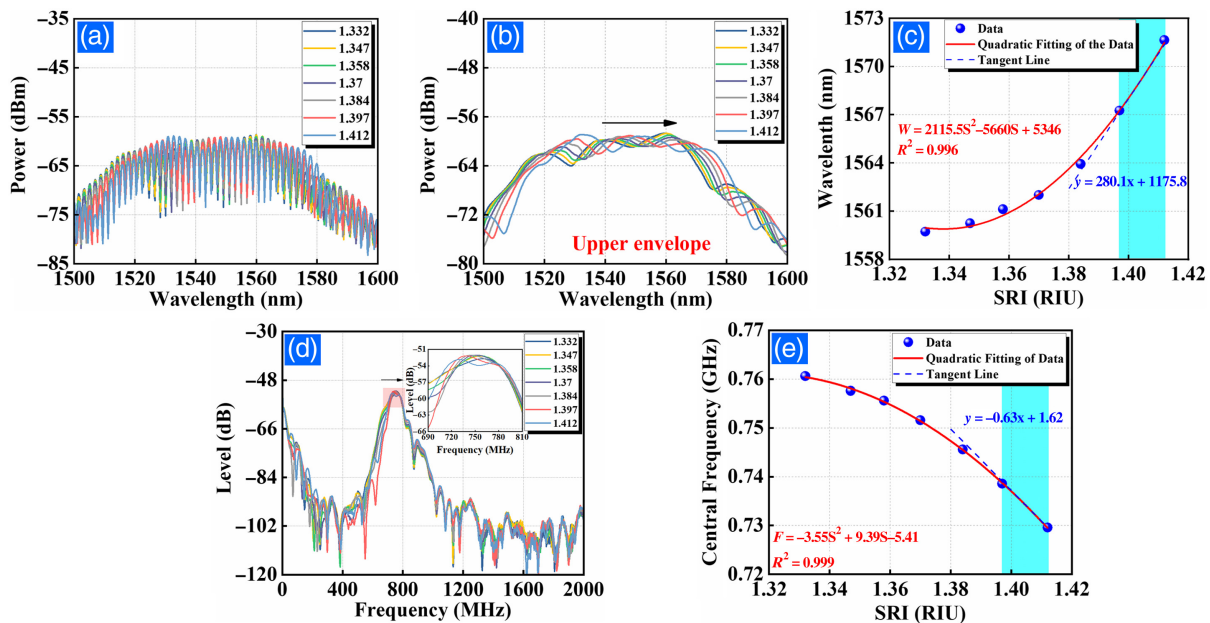


Fig. 3 (a) Transmission spectra and (b) the upper envelope changes of the cascaded interferometer under different SRIs with 20 mm TCF. (c) The quadratic fitting curve in the wavelength domain. (d), (e) The frequency responses of the sensor and the corresponding fitting curve, respectively. The blue-shaded region represents the linear region of the quadratic fitted curve within 1.397 – 1.412 RIU.

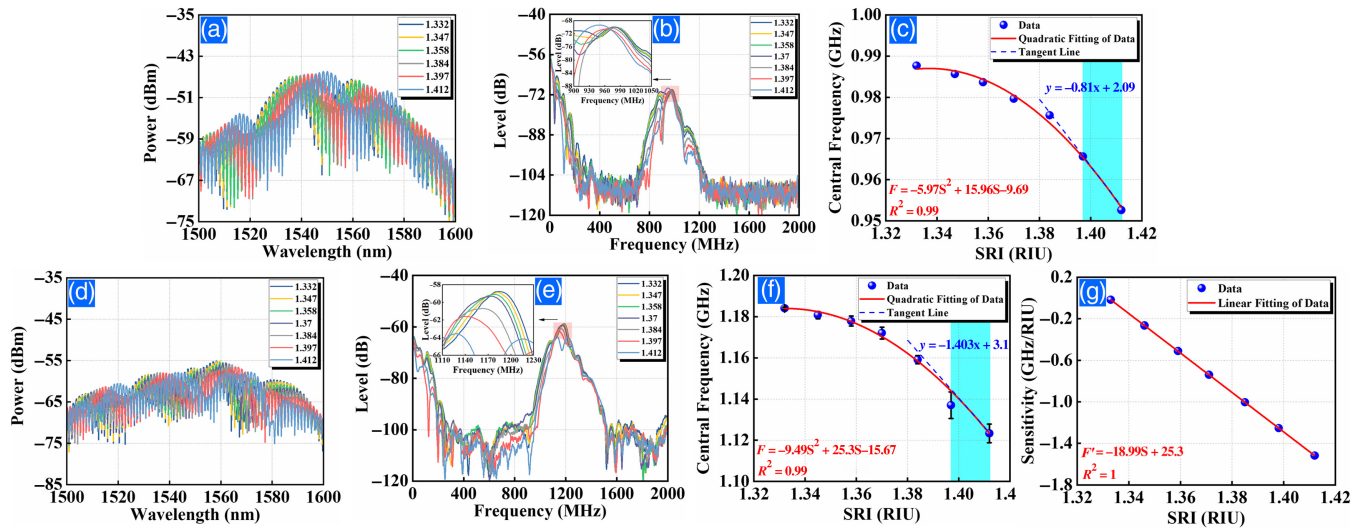


Fig. 4 (a), (d) Transmission spectra evolution of the proposed STNTS structure with different SRIs when TCF = 25 and 30 mm, respectively. (b), (e) The corresponding frequency responses. (c), (f) The quadratic fitting curves in the frequency domain. (g) The linear relationship between sensitivity and SRI. The blue-shaded region represents the linear region of the quadratic fitted curve within 1.397 – 1.412 RIU.

after processing with the upper envelope extraction method. The entire envelope is observed to redshift with an increase in SRI. By selecting 1559.5 nm as the demodulated wavelength, the quadratic fitting curve of the data points can be obtained, as illustrated in Fig. 3(c). The maximum theoretical wavelength sensitivity obtained by differentiating the quadratic function is ~ 280.1 nm/RIU in the range of 1.397 – 1.412 RIU. As mentioned above, to address problems stemming from traditional Vernier effect demodulation in the wavelength domain, a frequency domain demodulation method based on the MPF was adopted. Figures 3(d) and 3(e) present the frequency response and quadratic fitting curves of the sensor, respectively. The illustration in Fig. 3(d) clearly indicates that with an increase in SRI, the center frequency of the passband experiences a blue-shift, achieving a maximum theoretical frequency sensitivity of -0.63 GHz/RIU with good linearity.

As indicated by Eq. (6), the sensitivity of the proposed RI sensor is positively related to the length of the sensing fiber. To ensure a sufficiently low insertion loss for the sensor head, the length of NCF remains constant at 1 mm, meaning that the tapered fiber length stays unchanged. Figure 4 depicts the measured evolution of transmission spectra and frequency response of the proposed STNTS structure and the corresponding MPF with different SRIs when TCFs are 25 and 30 mm, respectively. On the one hand, the visibility of both transmission spectra exceeds 15 dB, and the entire modulated envelope exhibits a redshift trend. On the other hand, the center frequency of both passbands shifts to the lower frequency with an increase in SRI. Through quadratic function fitting of the experimental data, one can observe in Figs. 4(c) and 4(f) that the maximum theoretical RI sensitivity of the two sensors based on frequency demodulation can be derived from the curves. They are -0.81 GHz/RIU and -1.403×10^{-7} RIU within 1.397 – 1.412 RIU, respectively. The intermediate frequency (IF) of the VNA is set to 200 Hz, so the best resolution of the system can be calculated as 1.425×10^{-7} RIU.

The observed dual peaks in the frequency response of MPF are attributed to the sensor being formed by the cascade in-line interferometers, MMI, and MZI. Consequently, the system function incorporates two frequency components. In addition, when maintaining the length of the NCF constant at 1 mm, the passband's center frequency will move to a high frequency with an increase in the TCF length. Correspondingly, the maximum theoretical sensitivity increases, consistent with the theoretical analysis. Therefore, the proposed microwave photonic interrogation system based on STNTS structure exhibits the characteristic of tailorable sensitivity. To further demonstrate the significance of introducing a taper region for achieving high-sensitivity RI sensing, we also fabricated the STNTS structure with $N = 1$ mm and TCF = 30 mm with no taper; its frequency response is shown in Fig. 5(a). As the SRI increases from 1.332 to 1.412 RIU, the passband peak irregularly changes. Figure 5(b) shows the relationship between its data points and different SRIs, with a frequency change within the range of ± 3 MHz. This comparison underscores the advantageous role of the taper region in achieving more consistent and sensitive RI sensing.

3.2 Temperature Sensing Experiment and Stability Test

Temperature response is a crucial parameter for fiber-optic sensors as it often introduces cross-sensitivity problems to sensing systems. To assess the temperature sensing characteristics of the proposed sensing system with MPF based on the STNTS structure, the sensor with a TCF length of 30 mm was horizontally placed in a digital temperature control module with an accuracy of 0.01°C . In Fig. 6(a), the frequency response of the cascaded interferometer is depicted in the range of $25^\circ\text{C} - 75^\circ\text{C}$ with steps of 5°C . Notably, the central frequency of the passband exhibits minimal change with temperature. Figure 6(b) further illustrates that the passband frequency fluctuates within ± 1.5 MHz, resulting in a temperature-induced cross error of $\pm 1.05 \times 10^{-3}$ RIU, which is almost negligible compared with the SRI-induced

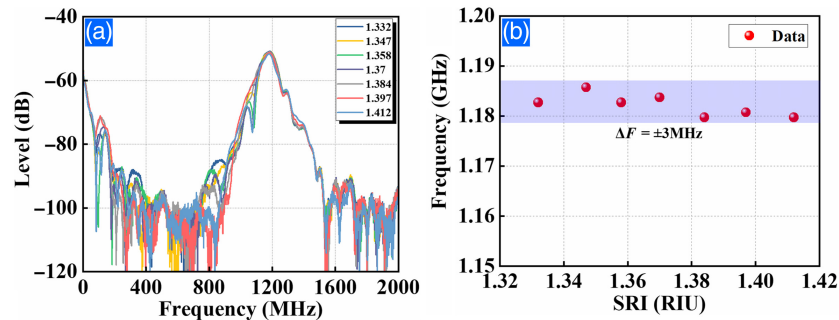


Fig. 5 (a) Frequency response of the proposed sensor with no taper and TCF = 30 mm. (b) The data points of central frequency change with different SRIs.

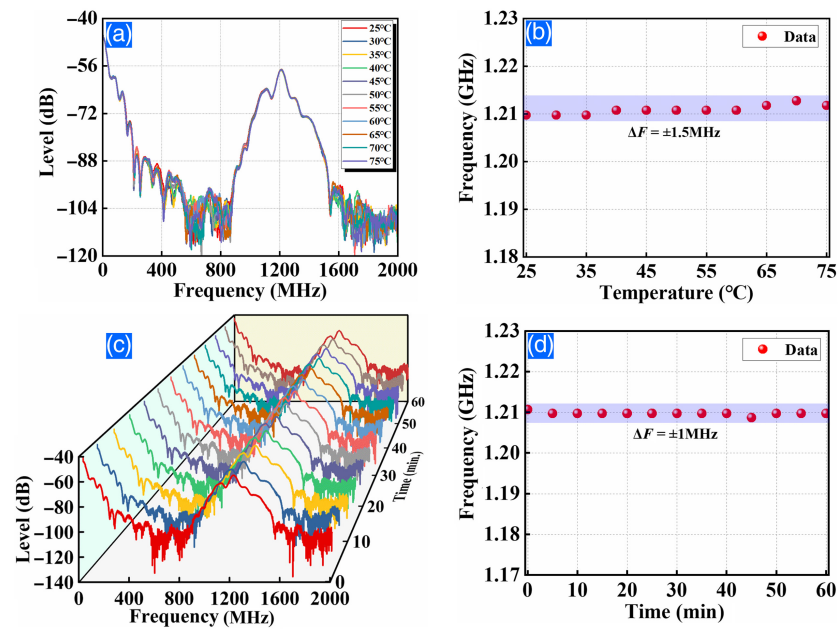


Fig. 6 (a) Frequency response of the MPF based on cascaded interferometer under different temperatures with 30 mm TCF. (b) The relationship between central frequency and temperature. (c), (d) The characteristic of stability within 1 h at $n = 1$.

frequency change. Hence, it can be inferred that the proposed MPIS is temperature-insensitive. Furthermore, we measured the stability of the system at 25°C within 1 h.

Figure 6(c) presents a three-dimensional diagram of the frequency response of the proposed sensing system when the TCF is 30 mm. Figure 6(d) shows the corresponding frequency fluctuation with the passband central frequency at 1.21072 GHz at ± 1 MHz, resulting in an ignorable measurement error of 7.01×10^{-4} RIU. Table 1 offers a comprehensive comparison of our work with other MPF-based RI sensing schemes. The proposed RI sensor stands out due to its remarkable advantage in high sensitivity. Furthermore, the chosen demodulation frequency is set at subgigahertz, enabling the utilization of a lower IF value (200 Hz). As a result, the resolution achieves an impressive value of 1.425×10^{-7} RIU, which is at least 6.3 times higher than those of reported previously. Notably, the system exhibits temperature insensitivity, eliminating the need for additional measures to address temperature cross-sensitivity issues. This characteristic significantly reduces system complexity and

cost, enhancing its application potential. Moreover, it is worth noting that in practical applications, interferometric optical fiber sensors must be physically packaged to shield them from external environmental interference to maintain performance. Besides, the length of TCF cannot be increased indefinitely because it would lead to an infinite decrease in the MZI's FSR, making it unable to generate a Vernier-like effect with the MMI. In addition, this would contradict the original intention of building a miniaturized and compact sensing system.

4 Conclusion

In conclusion, we have proposed and experimentally demonstrated an RI sensor implemented with a cascaded in-line interferometer-based MPF. The wavelength change induced by the SRI in the interference spectrum can be converted into a frequency shift of the MPF's central passband. With NCF and TCF lengths set at 1 and 30 mm, respectively, the maximum sensitivity and resolution can be calculated as -1.403 GHz/RIU and

Table 1 Comparison of the parameters of different RI sensing schemes.

Scheme	Sensitivity	Resolution (RIU)	Temperature Dependence	Ref.
MI	48.9 nm/RIU	2.04×10^{-4}	No	13
In-line-MZI	-59.9 nm/RIU	1.67×10^{-4}	No	14
In-line-MZI	178.2 dB/RIU	5.61×10^{-5}	No	15
Micro-FBG	11.9 GHz/RIU	2.63×10^{-5}	Yes	16
In-line-MZI	-1.1054 GHz/RIU	9×10^{-7}	Yes	18
EFPI	1.201 GHz/RIU	8.36×10^{-7}	No	19
Etched-PSFBG	0.53 GHz/RIU	1.9×10^{-6}	Yes	20
In-line-MZI	-1.403 GHz/RIU	1.425×10^{-7}	No	This work

Note: bold values distinguish this work from the work of others.

1.425×10^{-7} RIU. The sensitivity is also tailorable using different lengths of TCF. Moreover, the RI sensor exhibits temperature insensitivity within $25^{\circ}\text{C} - 75^{\circ}\text{C}$. Consequently, it can be considered that such an RI sensor with high sensitivity and high resolution has great application prospects in the fields of biomedicine and chemical industry.

Disclosures

The authors declare no competing financial interests.

Code and Data Availability

Data underlying the results presented in this paper are not publicly available at this time but may be obtained from the authors upon reasonable request.

Acknowledgments

This work was supported by the National Natural Science Foundation of China (Grant No. 61975167).

References

- W. Ning et al., “ Ω -shaped fiber optic LSPR biosensor based on mismatched hybridization chain reaction and gold nanoparticles for detection of circulating cell-free DNA,” *Biosens. Bioelectron.* **228**, 115175 (2023).
- S. Zhang et al., “Multichannel fiber optic SPR sensors: realization methods, application status, and future prospects,” *Laser Photonics Rev.* **16**(8), 2200009 (2022).
- A. Al Noman et al., “PCF based modal interferometer for lead ion detection,” *Opt. Express* **30**(4), 4895–4904 (2022).
- J. Guo et al., “High-sensitivity seawater salinity sensing with cladding etched fiber Bragg grating technology,” *IEEE Sens. J.* **23**(13), 14182–14192 (2023).
- S. Ciężczyk et al., “A wavelet derivative spectrum length method of TFBG sensor demodulation,” *Sensors* **23**(4), 2295 (2023).
- M. Lobry et al., “Plasmonic fiber grating biosensors demodulated through spectral envelopes intersection,” *J. Lightwave Technol.* **39**(22), 7288–7295 (2021).
- A. Celebanska et al., “Label-free cocaine aptasensor based on a long-period fiber grating,” *Opt. Lett.* **44**(10), 2482–2485 (2019).
- M. del Carmen Alonso-Murias, J. S. Velázquez-González, and D. Monzón-Hernández, “SPR fiber tip sensor for the simultaneous measurement of refractive index, temperature, and level of a liquid,” *J. Lightwave Technol.* **37**(18), 4808–4814 (2019).
- F. Chiavaioli and D. Janner, “Fiber optic sensing with lossy mode resonances: applications and perspectives,” *J. Lightwave Technol.* **39**(12), 3855–3870 (2021).
- F. Chiavaioli et al., “Femtomolar detection by nanocoated fiber label-free biosensors,” *ACS Sens.* **3**(5), 936–943 (2018).
- T. Zhu et al., “Gold-coated optical fiber supermode interferometer for insulin bio-sensing,” *Opt. Laser Technol.* **168**, 109878 (2024).
- M. Shao et al., “Refractive index sensing of SMS fiber structure based Mach-Zehnder interferometer,” *IEEE Photonics Technol. Lett.* **26**(5), 437–439 (2014).
- Y. Li, G.-F. Yan, and S. He, “Thin-core fiber sandwiched photonic crystal fiber modal interferometer for temperature and refractive index sensing,” *IEEE Sens. J.* **18**(16), 6627–6632 (2018).
- H. Wang et al., “Miniature fiber-optic near-surface gap-coupled cladding waveguide Mach-Zehnder interferometric refractive index sensor inscribed by femtosecond laser,” *Opt. Laser Technol.* **166**, 109649 (2023).
- F. Mumtaz, Y. Dai, and M. A. Ashraf, “Inter-cross de-modulated refractive index and temperature sensor by an etched multi-core fiber of a MZI structure,” *J. Lightwave Technol.* **38**(24), 6948–6953 (2020).
- Y. Cao et al., “Resolution-improved refractive index sensing system based on microwave photonic filter and microfiber grating,” in *14th Int. Conf. Opt. Commun. and Networks (ICOON)*, IEEE, pp. 1–3 (2015).
- J. Liu et al., “On-chip sensor for simultaneous temperature and refractive index measurements based on a dual-passband microwave photonic filter,” *J. Lightwave Technol.* **36**(18), 4099–4105 (2018).
- Y. Zhang et al., “High-sensitivity and high-resolution RI sensor with ultrawide measurement range based on NCF with large offset splicing and MPF interrogation,” *IEEE Sens. J.* **22**(23), 22707–22713 (2022).
- S. Zheng et al., “A refractive index sensing system by using EFPI based microwave photonic filter,” in *21st Int. Conf. Opt. Commun. and Networks (ICOON)*, IEEE, pp. 1–3 (2023).
- Y. Cao et al., “High-resolution and temperature-compensational HER2 antigen detection based on microwave photonic interrogation,” *Sens. Actuators, B* **245**, 583–589 (2017).
- Q. Shi et al., “Resolution-enhanced fiber grating refractive index sensor based on an optoelectronic oscillator,” *IEEE Sens. J.* **18**(23), 9562–9567 (2018).
- X. Cai, X. Chen, and H. Fu, “A temperature sensing scheme realized with Sagnac interferometer based microwave photonic filter,” in *18th Int. Conf. Opt. Commun. and Networks (ICOON)*, IEEE, pp. 1–3 (2019).
- H. Liao et al., “Sensitivity amplification of fiber-optic in-line Mach-Zehnder interferometer sensors with modified Vernier-effect,” *Opt. Express* **25**(22), 26898–26909 (2017).
- J. Tian et al., “High-sensitivity fiber-optic strain sensor based on the Vernier effect and separated Fabry-Perot interferometers,” *J. Lightwave Technol.* **37**(21), 5609–5618 (2019).
- Z. Tian and S. S.-H. Yam, “In-line single-mode optical fiber interferometric refractive index sensors,” *J. Lightwave Technol.* **27**(13), 2296–2306 (2009).

Xun Cai is currently pursuing a PhD in the Department of Electronics Engineering, Xiamen University, Xiamen, China. His current research interests include fiber-optic sensors, fiber laser sensors, and terahertz signal generation.

Yi Zhuang is currently pursuing a master's degree in the Department of Electronics Engineering, Xiamen University, Xiamen, China. His research interests include fiber-optic sensors based on microwave photonics technology.

Tongtong Xie is currently pursuing a PhD in the Department of Electronics Engineering, Xiamen University, Xiamen, China. Her current research interests include fiber-optic sensing technology and signal generation technology based on microwave photonics.

Shichen Zheng received his master's degree from the Department of Electronics Engineering, Xiamen University, Xiamen, China. His research interests include fiber-optic sensors based on microwave photonics technology.

Hongyan Fu received her PhD in optical engineering from Zhejiang University, Hangzhou, China, in 2010. She is currently a professor of the Department of Electronic Engineering, Xiamen University, Xiamen, China. Her research interests include fiber-optic sensors, fiber-based devices, and microwave photonics.